REPORT DOCUMENTATION PAGE

Form Approved
OMB No. 0704-0188

1. REPORT DATE *(DD-MM-YYYY)*	2. REPORT TYPE	3. DATES COVERED *(From - To)*
June 2006	Published Journal Article	January 2003- October 2008

4. TITLE AND SUBTITLE

Dynamic Bidirectional Reflectance Distribution Functions. Part II – Mathematical Representation Model

5a. CONTRACT NUMBER
F41624-02-D-7003

5b. GRANT NUMBER

5c. PROGRAM ELEMENT NUMBER
63231F

6. AUTHOR(S)
Albert W. Bailey, Edward A. Early, Kenneth K. Keppler, Victor I. Villavicencio, Justin J. Zohner, Robert J. Thomas, Paul Kennedy, George Megaloudis

5d. PROJECT NUMBER
5020

5e. TASK NUMBER
D2

5f. WORK UNIT NUMBER
03

7. PERFORMING ORGANIZATION NAME(S) AND ADDRESS(ES)

Air Force Research Laboratory
Human Effectiveness Directorate
Directed Energy Bioeffects Division
Optical Radiation Branch
2624 Louis Bauer Dr.
Brooks City-Base, TX 78235-5128

Northrop Grumman-IT
4241 Woodcock Dr., Ste B-100
San Antonio, TX 78228

8. PERFORMING ORGANIZATION REPORT NUMBER

9. SPONSORING / MONITORING AGENCY NAME(S) AND ADDRESS(ES)

Air Force Research Laboratory
Human Effectiveness Directorate
Directed Energy Bioeffects Division
Optical Radiation Branch
2624 Louis Bauer Dr.
Brooks City-Base, TX 78235-5128

10. SPONSOR'S/MONITOR'S ACRONYM(S)
AFRL/HEDO

11. SPONSOR'S/MONITOR'S REPORT NUMBER(S)
AFRL-HE-BR-JA-2006-0022

12. DISTRIBUTION / AVAILABILITY STATEMENT
APPROVED FOR PUBLIC RELEASE; DISTRIBUTION UNLIMITED. Other requests for this document shall be referred to AFRL/HEDM, 8262 Hawks Road, Brooks City-Base, Texas 78235. Case file no. 06-294, 21 Aug 06.

13. SUPPLEMENTARY NOTES
Contract Monitor – Maj Lawrence Schad. **Published in Journal of Laser Applications Vol 20, no. 1, Feb 2008**

14. ABSTRACT
Two currently fielded laser eye protection devices (LEP) use a reflective technology to block laser threats outside of the visible spectrum: WD1A and DADS. In addition to the reflective dielectric stack, the DADS LEP includes a dye to provide protection against a green laser. The high transmittance of non-threat, visible wavelengths by these two LEP makes them well suited for aircrew at night. METHODS: Two approaches to extend the same laser protection to aircrew requiring spectacle correction were investigated: 1) adding a prescription to the LEP and 2) formatting the LEP into a clip-on to attach over a regular prescription spectacle. Three experiments were conducted to compare the effects of the protection (WD1A vs. DADS) and approaches (scripted LEP vs. clip-on's) on 1) Regan contrast acuity under room illumination with and without glare, 2) the distractibility of multiple reflections, and 3) night vision goggle (NVG) acuity. Two emmetropes were also tested with non-prescription LEP for comparison. RESULTS: In general, both approaches were very promising. With the scripted LEP format, only small decrements were found for contrast acuity with glare, multiple reflections with clear visors, and NVG acuity. With the clip-on format, only small decrements were found for emmetrope contrast acuity with glare. In addition, small decrements were found on the multiple reflections test for both ametropes and emmetropes. The clip-on format may provide agile protection with minimal operational impact. Refinements in the process of adding prescriptions to LEP may also minimize their operational impact.

15. SUBJECT TERMS
prescription laser eye protection, contrast acuity, glare, internal reflections, night vision goggles

16. SECURITY CLASSIFICATION OF:			17. LIMITATION OF ABSTRACT	18. NUMBER OF PAGES	19a. NAME OF RESPONSIBLE PERSON
a. REPORT	b. ABSTRACT	c. THIS PAGE			Dr. Edward A. Early
Unclassified	Unclassified	Unclassified	UU	16	19b. TELEPHONE NUMBER *(include area code)*

Standard Form 298 (Rev. 8-98)

Dynamic bidirectional reflectance distribution functions: Measurement and representation

Albert W. Bailey, Edward A. Early, Kenneth S. Keppler, and Victor I. Villavicencio
Northrop Grumman, 4241 Woodcock Drive, Suite B-100, San Antonio, Texas 78238

Paul Kennedy, Robert J. Thomas, and Justin J. Zohner
Human Effectiveness Directorate, Directed Energy Bioeffects Division, Optical Radiation Branch, Air Force Research Laboratory, 2624 Louis Bauer Drive, Brooks City-Base, Texas 78235

George Megaloudis
Northrop Grumman, 100 Brickstone Square, Andover, Massachusetts 01810

(Received 11 October 2006; accepted for publication 8 February 2007; published 16 January 2008)

With high-energy lasers, not only the direct laser beam can pose significant eye and skin hazards, but also light reflecting off material illuminated by the beam. Proper hazard analysis for a material irradiated by a laser relies upon the reflecting properties of the material surface, as these properties determine the magnitude and direction of the reflected laser energy commonly characterized by the bidirectional reflectance distribution function (BRDF). However, a high-energy laser heating and possibly melting a material can change the reflecting properties of that material, so these changes must be included in the hazard analysis. Traditional methods for measuring the BRDFs of materials are not practical for measurement of materials with rapidly-changing surface properties. However, BRDF measurement by imagery of a witness screen allows for practical measurements of the dynamically-changing BRDFs of materials under high-energy laser irradiation. Using this technique, the dynamic BRDFs of stainless steel and copper were measured under high irradiance. The BRDF of the materials was observed to change in magnitude, width, and the specular direction. In some instances, this would result in an increase in exposure to the laser radiation for some observers over that which would be predicted using static BRDF measurements where the reflective characteristics of the material are assumed to be constant. For effective use in safety calculations, the dynamic BRDFs need to be represented in a form suitable for use in safety analysis codes. Construction of a dynamic BRDF representation is complicated by the fact that data cannot be practically obtained over the entire range of incident and reflected angles or for all points in time. Therefore, a technique is required for interpolating through regions of missing data. A BRDF representation form has been developed based on expansions in spherical harmonics in a transformed coordinate space. The efficacy of this representation is examined using experimental data on stainless steel and copper samples exposed to high-energy laser irradiation. The representation technique is found to be capable of robust predictions at all incident and reflected angles and at interpolated material states. Simplified "envelope" models based on these representations are suitable for inclusion in laser safety codes for predicting reflection hazards from high-energy lasers. © *2008 Laser Institute of America.*

Key words: reflectance, bidirectional reflectance distribution function (BRDF), spherical harmonics, high-energy laser

I. INTRODUCTION

With low-energy lasers, only the direct beams or highly specular reflections of the beams pose hazards. With multikilowatt high-energy lasers, even less than fully specular reflections can be eye and skin hazards at substantial distances from the reflecting surface. For proper laser safety, it is important to determine the magnitude of these reflections and how they vary as a function of time when materials irradiated by high-energy lasers change their reflection properties upon heating and melting.

In the coarsest approximation, light reflections can be treated either as specular (angle of reflection equal to the angle of incidence) or Lambertian (equal reflected radiance at all viewing angles). For a typical material, which is neither totally specular nor Lambertian, the former approximation will result in Nominal Ocular Hazard Distance (NOHD) estimates that are much larger than the actual NOHD, while the latter approximation will underestimate the true NOHD. In order to provide more accurate hazard predictions, the scattering of light must be represented in terms of a BRDF (bidirectional reflectance distribution function), which characterizes the ratio between the reflected radiance to the incident irradiance. The BRDF can be written as[1]

$$\text{BRDF} = f_r(\theta_i, \phi_i, \theta_r, \phi_r) = \frac{\delta L_r}{\delta E_i} = \frac{\delta \Phi_r / \delta A \cos(\theta_r)\delta\omega}{\delta \Phi_i / \delta A} \ (\text{sr}^{-1}), \quad (1)$$

where
δL_r=differential reflected radiance from a flat surface $[\text{W}/(\text{m}^2\text{-sr})]$
δE_i=differential incident irradiance onto a flat surface (W/m^2)
$\delta \Phi_i$=power incident upon the differential area δA (W)
$\delta \Phi_r$=power reflected into the differential solid angle $\delta\omega$ from the area δA (W)
θ_i=polar angle of the incident light
ϕ_i=azimuthal angle of the incident light
θ_r=polar angle of the reflected light
ϕ_r=azimuthal angle of the reflected light
δA=differential surface area $\delta\omega$ differential solid angle (sr).

In currently used laser safety models, the BRDF characterizing a material at a particular wavelength has been assumed to be unchanging. For low to moderate power lasers, this is appropriate. However, high-energy lasers will alter the physical properties of the surfaces they strike. The material will become hot and may burn or melt, which may dramatically alter the BRDF of the material. To properly model the reflection hazards in this situation, one needs to model dynamic BRDFs, which is a challenging requirement. Instead of characterizing the surface reflections at one set of incident and reflected angles at a time and producing an expression which is good for all circumstances, one must rapidly characterize reflections for all incident and reflected angles and produce a representation capable of reproducing this behavior for all states of the material.

Reflection measurements are normally made using gonioreflectometers (also called scatterometers), which measure the reflected light for a single incident and reflected angle combination at a time.[2–8] Minutes to hours are typically required for sufficient measurements to properly characterize the BRDF of a material at a given wavelength. Because of the long measurement times involved, this technique is obviously inapplicable to the situation where the surface properties are rapidly changing.

Direct imaging of samples is a different technique that has been used for determining BRDF. By illuminating a cylindrical or spherical sample and observing the sample with an imaging device, it is possible to obtain data for many angles of incidence from a single image.[9–11] This technique allows for fast surveys of the BRDF but is limited to materials with isotropic surfaces that can be obtained in a spherical or other curved form without altering their reflective or heating characteristics. A variation of this technique is to use multiple illumination directions and multiple viewing positions, interpolating to determine the BRDF at intermediate points. This permits the measurement of complex objects under natural as well as laboratory settings.[12–14] This technique has recently been used for measurement of dynamic BRDFs of burning, drying, and corroding materials, with time variation over the scale of minutes to hours.[15] However, since there is only one angle of reflection recorded for each angle of incidence for a given viewing angle, multiple viewing locations are needed to construct a full BRDF, and the technique is not accurate with highly specular materials.

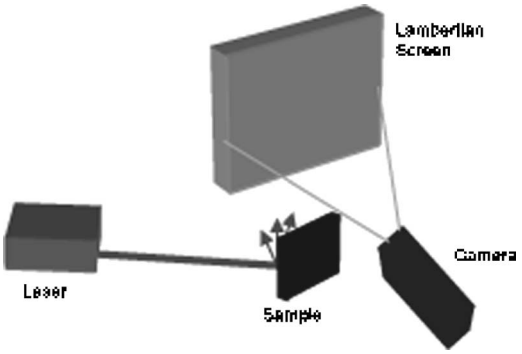

FIG. 1. BRDF measurement with scatter screen IR imagery.

A method that captures the reflection pattern for many viewing angles as a snapshot in time is required. A technique that satisfies this requirement is imaging the scattered light onto a Lambertian screen, so that the reflectance at many angles can be captured at once, as shown schematically in Fig. 1. Using a camera to image the screen also allows recording the changes in the BRDF as a function of time as the surface reflectance properties change in response to the laser heating the sample.

This technique of imaging a Lambertian screen is a variant of the method in which a hemisphere is imaged in its entirety using a fisheye or by directing the camera at a curved mirror placed beside the target.[16,17] Partial imaging has also been performed using more conventional optics.[18,19] Variations on this scheme use a parabolic mirror to reflect the light to a viewing camera[20] or use fiber optics to illuminate the sample and feed light back to the camera.[21] However, in order to allow the use of high-energy lasers and to allow access to the sample by additional instrumentation, a flat screen was used, allowing measurement of the reflected light over a more limited angular range.

With the Lambertian screen technique used in these experiments, each test allows measurement of only a single incident angle and a limited range of reflected angles, so multiple tests must be conducted to sample the BRDF effectively. Even with multiple tests, the sample space is limited and so it is necessary to use some model to extrapolate and interpolate from the available data to predict reflections for situations that have not been measured exactly. A mathematical model to represent these BRDFs is described in Sec. IV.

II. MEASUREMENT GEOMETRY

The essential elements of the measurement of sample dynamic BRDF by Lambertian screen imagery are schematically depicted in Fig. 2. For a fixed laser direction of incidence (specified by the angles θ_i and ϕ_i), the radiance reflected by the material exhibits an angular distribution that is determined by the BRDF of the material. With high-energy lasers, the surface properties will change due to the laser irradiation, and so the BRDF will depend on its temperature and the time required to raise it to that temperature. The

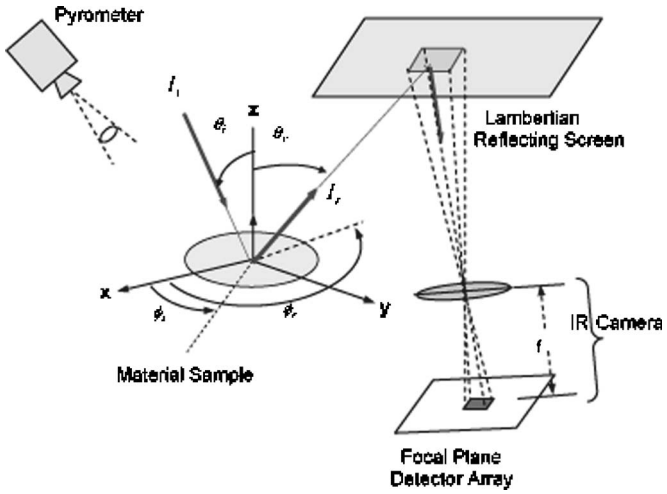

FIG. 2. Dynamic BRDF measurement approach.

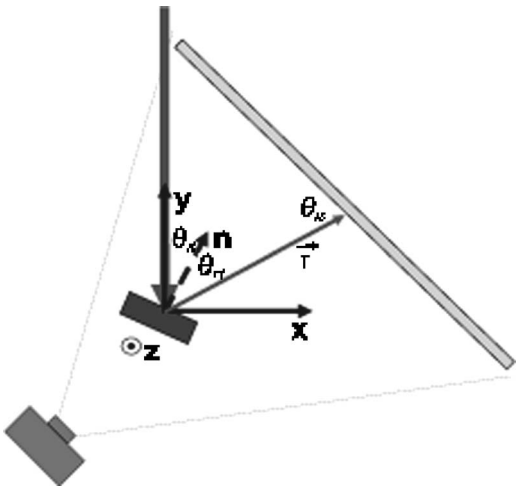

FIG. 3. Lab coordinate system for BRDF measurements.

BRDF, therefore, needs to be determined as a function of this time-temperature history. The angular distribution of the reflected radiance gives rise to a spatially varying pattern of irradiance at the surface of the Lambertian screen. This irradiance is imaged by a camera onto a camera's focal plane array. Figure 2 shows a representative detector element in this array and the region on the Lambertian screen imaged onto this detector by the camera optics. The output of this detector is proportional to the reflected radiance and, hence, the material's BRDF at the laser's direction of incidence and the unique direction of reflection specified by the angles θ_r and ϕ_r. Therefore, a single camera image provides simultaneous measurements that can be used to estimate the BRDF at a large number of discrete reflection directions for a given angle of incidence and sample temperature.

The relationship between the reflected irradiance incident on the Lambertian screen and detector output counts is established through a separate calibration procedure described in Sec. III. As shown, this measurement approach also uses a narrow field-of-view pyrometer (or pyrometers) that independently measures sample temperature during the irradiation interval. The pyrometer and the camera are time-synchronized so that data from each camera image can be accurately correlated with the sample temperature measurements from the pyrometer. For the specified laser angle of incidence, a sequence of camera images is collected at the camera frame rate during the laser irradiation interval and stored for subsequent processing. The measurement process is then repeated at other angles of incidence and all collected data are processed as described in Sec. III to characterize dynamic BRDF of the illuminated sample.

In this measurement technique the screen and camera together are considered to be the receiver, so the reflecting properties of the screen and a radiance calibration of the camera are not needed explicitly. The signal from the camera is proportional to the radiance reflected by the screen which, in turn, is proportional to the irradiance incident upon the screen. The irradiance incident at the screen, E_{is}, is related to the radiance reflected from the sample, I_{rt}, by

$$E_{\mathrm{is}} = L_{\mathrm{rt}} \times \omega_o \times \cos(\theta_{\mathrm{is}}), \tag{2}$$

where θ_{is} is the incident polar angle at the screen and ω_0 is the projected solid angle from the screen to the illuminated area of the sample, given by

$$\omega_o = \frac{A_t}{r^2} \times \cos(\theta_{\mathrm{rt}}). \tag{3}$$

The illuminated area of the sample is A_t, the distance from the center of the illuminated area of the sample to the location on the screen is r, and the reflected polar angle from the sample normal is θ_{rt} (Fig. 3). Here it is assumed that the illuminated area on the sample and the area of observation on the screen are sufficiently small compared to the distance from the sample to the screen and that the angle θ_{rt} is well defined. In order for the approximation to be off by about 1% or less, the distance needs to be at least 20 times the spot size.[22] In these experiments, the distance was more than 100 times the spot size, so the angle was well defined.

The irradiance incident on the sample is

$$E_{\mathrm{it}} = \frac{\Phi}{A_t}, \tag{4}$$

where Φ is the incident laser power. So using Eqs. (2) and (4) the BRDF can be written as

$$f_r \equiv \frac{L_{\mathrm{rt}}}{E_{\mathrm{it}}} = \frac{E_{\mathrm{is}}}{\Phi} \frac{r^2}{\cos(\theta_{\mathrm{is}})\cos(\theta_{\mathrm{rt}})}. \tag{5}$$

III. MEASUREMENT CALIBRATION

To relate measured signals to BRDF, a number of steps are required. The first is to determine positions of the points on the Lambertian screen associated with each of the pixels of the camera. For simplicity, a coordinate system is chosen where the center of the laser spot on the sample is used as the origin, the *y*-axis points along the incident laser beam path, and the *z*-axis is vertical, as shown in Fig. 3. The *x*-*y*-*z* locations of the upper left ($\mathbf{r}_{\mathrm{ul}}$), upper right ($\mathbf{r}_{\mathrm{ur}}$), and lower left ($\mathbf{r}_{\mathrm{ll}}$) corners of the screen are measured. The camera is placed with the field of view normal to the screen and ori-

ented so that there is no skew of the camera orientation relative to the screen. The pixel row numbers, i_{top} and i_{bottom}, for the top and bottom of the screen are noted, as are the column numbers, j_{left} and j_{right}, for the left and right edges of the screen. (Note that by convention, the [0,0] pixel is in the upper-left corner of the camera visual field.) The *x*-*y*-*z* location in space of the portion of the screen imaged by a pixel in the *i*th row and *j*th column of the detector array can be computed as

$$\mathbf{r}(i,j) = \mathbf{r}_{\text{ul}} + (i - i_{\text{top}})\left(\frac{\mathbf{r}_{\text{ll}} - \mathbf{r}_{\text{ul}}}{i_{\text{bottom}} - i_{\text{top}}}\right) + (j - j_{\text{left}})\left(\frac{\mathbf{r}_{\text{ur}} - \mathbf{r}_{\text{ul}}}{j_{\text{right}} - j_{\text{left}}}\right). \tag{6}$$

This relates the pixel indices to the spatial coordinates, but the calibration of the detector counts to material BRDF must still be derived.

Consider a calibration location, $\mathbf{r}_C(i_C, j_C)$, at some point on the screen. Let the irradiance E_C at the calibration location be measured using a power meter and detector (with known aperture area) oriented normal to the screen. By observing the detector location with the camera and then noting the counts, U_C, at that position $[\mathbf{r}_C(i_C, j_C)]$ with the detector removed, the screen-lens-camera response factor at the calibration point can be calculated as

$$R_C = \frac{U_C}{E_C}, \tag{7}$$

where any background offset to the counts has been subtracted before calculating U_C. With a perfectly Lambertian screen and a camera lens with no light falloff toward the corners of the frame, the responsivity would be the same for every camera pixel. With a real system, adjustments are required for proper calibration over the full image. The responsivity for other points on the screen can be determined by placing an isotropic point source of light (an incandescent bulb was used) at the origin. At the calibration point, the irradiance of the screen will be

$$E_C^P = \frac{U_C^P}{R_C} = E_C \frac{U_C^P}{U_C}, \tag{8}$$

where U_C^P is the detector counts at the calibration point under these conditions. The responsivity associated with an arbitrary pixel (i,j) will be

$$R(i,j) = \frac{U(i,j)}{E(i,j)}, \tag{9}$$

where $U(i,j)$ are the detector counts for that pixel and $E(i,j)$ is the irradiance for the part of the screen imaged by that pixel.

Now, for an isotropic point source, the irradiance variation over the screen will depend upon the distance from the sample to the screen as $1/r^2$ and the angle as $\cos(\theta_{\text{is}})$, so the irradiance at an arbitrary pixel (i,j) will be

$$E^P(i,j) = E_C^P \frac{r_C^2 \cos(\theta_{\text{is}})_C}{r^2(i,j)\cos(\theta_{\text{is}}(i,j))} = E_C^P \frac{r_C^3}{r^3(i,j)}. \tag{10}$$

If the detector response is linear with irradiance, then with any illumination

$$E(i,j) = E^P(i,j)\frac{U(i,j)}{U^P(i,j)} = E_C^P \frac{U(i,j)}{U^p(i,j)} \frac{r_C^3}{r^3(i,j)}, \tag{11}$$

where $U^P(i,j)$ is the detector counts for pixel (i,j) with the point source. Substituting Eq. (8) gives

$$E(i,j) = E_C \frac{U_C^P U(i,j)}{U_C U^p(i,j)} \frac{r_C^3}{r^3(i,j)}. \tag{12}$$

Using this value in Eq. (9) gives

$$R(i,j) = \frac{1}{E_C} \frac{U^{P^*}(i,j) U_C}{U_C^P} \frac{r^3(i,j)}{r_C^3}. \tag{13}$$

During a test the irradiance on the screen for any pixel can be calculated as

$$E_{\text{is}}(i,j) = \frac{U(i,j)}{R(i,j)}. \tag{14}$$

Substituting this value into Eq. (5) gives the BRDF as

$$f_r(\theta_{\text{it}}, \hat{r}(i,j)) = \frac{1}{\Phi} \frac{U(i,j)}{R(i,j)} \frac{r^2(i,j)}{\cos(\theta_{\text{is}}(i,j))\cos(\theta_{\text{rt}}(i,j))}, \tag{15}$$

where $\hat{r}(i,j)$ is the direction vector towards the point on the screen image by the pixel in row *i* and column *j*. Using the expression for $R(i,j)$ in Eq. (13) yields

$$f_r(\theta_{\text{it}}, \hat{r}(i,j)) = \frac{E_C}{\Phi} \frac{U(i,j) U_C^P}{U^P(i,j) U_C} \frac{r_C^3}{r(i,j)} \times \frac{1}{\cos(\theta_{\text{is}}(i,j))\cos(\theta_{\text{rt}}(i,j))}, \tag{16}$$

where

E_C=Irradiance at the calibration location when the screen is illuminated by the calibration source

Φ=Laser power incident upon the sample

$U(i,j)$ =Detector counts for pixel i,j

U_C^P =Detector counts of the pixel imaging the calibration location when the screen is illuminated by a point source

U_C=Detector counts of the pixel imaging the calibration location when the screen is illuminated by the calibration source

$r(i,j)$=Distance from the sample to the portion of the screen imaged by pixel i,j

r_C=Distance from the sample to the calibration location on the screen

$\theta_{\text{is}}(i,j)$=Angle relative to the screen normal of light rays from the sample illuminating the portion of the screen imaged by pixel i,j

$\theta_{\text{rt}}(i,j)$=Angle relative to the sample normal of light rays from the sample illuminating the portion of the screen imaged by pixel i,j.

IV. BRDF FITTING AND INTERPOLATION TECHNIQUE

A. Background

A common method of modeling the BRDF of a surface is to make assumptions about the physical nature of the surface reflections and parameterize the solution based on these assumptions. This technique generally notes the roughness of surfaces and ascribes the imperfect specularity as due to variations in the surface normal on a microscopic scale.[23–26] A widely used model of this type is the Maxwell-Beard model, for which significant databases of material reflection parameters exist.[27,28] This model has been used extensively for applications where values of the actual reflected irradiance are paramount. (The majority of reflection modeling is for the rendering of computer graphics.) The model has the advantage of requiring only reflection measurements in the plane defined by the incident ray and the macroscopic surface normal to fully characterize the BRDF. More sophisticated models with a basis in physical optics, rather than geometrical optics, are also beginning to be widely used.[29,30]

While physically-based models have been quite successful for modeling certain classes of materials, they fail on others due to the complexity of light interaction with real-world surfaces. The alternative is empirical modeling which treats the surface reflections phenomenologically, without attempting to model the details of the underlying surface physics. The simple model developed by Phong was an early one of this type, still widely used for computer graphics, which models specular reflections as a cosine lobe.[31] More complex variations with more parameters have proven capable of modeling reflections as accurately as the best physical models.[32]

The simplest way to represent a BRDF would be as a table of values for each incident and reflected angle. This approach has the obvious advantage that it is trivially applicable to any type of surface, with no pre-assumptions as to the reflection characteristics of the surface. A common reason that BRDF models are used instead of this more direct approach is the enormous volume of data that direct tabulation implies. The BRDF is a function of both the polar and azimuthal coordinates of the incident ray and reflected rays, which is a four-dimensional parameter space. Also, this space cannot be sampled too coarsely or the specular peaks will be missed. Moving to dynamic BRDFs makes the situation even more difficult as now data must be stored for the material at different stages of irradiation. Potentially, one is talking about gigabytes of data needed to characterize a single dynamic BRDF at a single wavelength. Some thoughtful data fitting techniques can do much to reduce the measurement and storage requirements.

B. Angular coordinate transformation

A change of coordinates can do a great deal to reduce the required storage. Instead of using the incident angle (θ_i, ϕ_i) and the reflected angle (θ_r, ϕ_r), one can parameterize the BRDF in terms of the angular coordinates of a vector halfway between the incidence vector and the reflection vector, θ_h, and the difference angle between this halfway vector and the incidence vector, θ_d (Fig. 4). Parameterizing in the difference polar angle allows characterization of Fresnel reflectance changes and retroreflection. The remaining variation with azimuthal difference angle, ϕ_d, is only a weak function of the incident angle. For isotropic materials there is no variation in the BRDF with the azimuthal halfway angle, ϕ_h. Additionally, we can scale the BRDF by the cosines of the incident and reflected angles. The BRDF then becomes only a weak function of the angle of incidence.[33] The actual function to be fit is thus

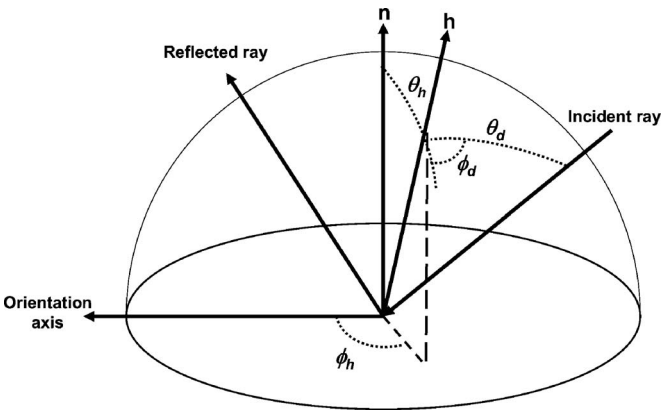

FIG. 4. The transformed coordinates in terms of the halfway angle θ_h, ϕ_h and the difference angle θ_d, ϕ_d.

$$\tilde{f}_r(\theta_h, \phi_h, \theta_d, \phi_d) = \cos(\theta_i)\cos(\theta_r) f_r(\theta_i, \phi_i, \theta_r, \phi_r). \tag{17}$$

Using this coordinate transformation makes the experimental requirements easier: measurements at fewer angles of incidence are required to characterize the BRDF of a material. In this transformed space, the specular peak is always at $\theta_h = 0$ and the retroreflective peak at $\theta_d = 0$. Fine resolution is needed only for small angles; larger angles can be characterized more coarsely. The azimuthal difference angle, ϕ_d, can be characterized quite coarsely and the azimuthal half-way angle, ϕ_h, is ignorable for isotropic materials.

The conversion from the regular coordinate system to the transformed coordinate system is accomplished through a series of intermediate coordinate transformations. First the coordinate frame is transformed so that the incident azimuthal angle is always at 180° (the situation when the sample grooving is horizontal and the sample is not tilted) giving

$$\tilde{\phi}_r = \phi_r + (\pi - \phi_i). \tag{18}$$

This coordinate system is then rotated about the normal to the plane of incidence so that the incident angle is at the pole, that is,

$$\tilde{\boldsymbol{\omega}} = R_y(\tilde{\boldsymbol{\omega}}_r(\theta_r, \tilde{\phi}_r), -\theta_i), \tag{19}$$

where $\boldsymbol{\omega}$ is the vector angle defined by θ and ϕ, and R is defined such that

$$R_y(\boldsymbol{\omega}(\theta,\phi),\vartheta)=\begin{bmatrix}\cos(\vartheta) & 0 & -\sin(\vartheta)\\ 0 & 1 & 0\\ \sin(\vartheta) & 0 & \cos(\vartheta)\end{bmatrix}\begin{bmatrix}\sin(\theta)\cos(\phi)\\ \sin(\theta)\sin(\phi)\\ \cos(\theta)\end{bmatrix}. \tag{20}$$

In this rotated frame (designated by the prime mark)

$$\theta_h'=\frac{\theta_r'}{2} \tag{21}$$

and

$$\phi_h'=\tilde{\phi}_r-\tilde{\phi}_i=\tilde{\phi}_r-(\pi-\phi_i). \tag{22}$$

Also, here the difference angles are easily set as

$$\theta_d'=\theta_i \tag{23}$$

and

$$\phi_d'=\phi_i-\phi_h'. \tag{24}$$

The halfway and difference angles in the unprimed frame can then be obtained as

$$\boldsymbol{\omega}=R_y(\boldsymbol{\omega}',\theta_i). \tag{25}$$

C. Spherical harmonic representations

For a given incident angle (and sample orientation for anisotropic media) the transformed BRDF values as a function of the halfway angle and difference angle can simply be tabulated, using finer intervals near $\theta=0$ to capture the specular peak. However, a better approach is to characterize the BRDF angular variation using an expansion in terms of orthogonal functions such as spherical harmonics.[34,35] Spherical harmonics are a set of orthogonal functions that can be used to map function values in a spherical coordinate system. Any function $f(\theta,\phi)$ can be approximated to any degree of required accuracy as a sum of terms of these harmonic functions, Y_l^m, that is,

$$f(\theta,\phi)\equiv\sum_{l=0}^{\infty}\sum_{m=-l}^{l}A_l^mY_l^m(\theta,\phi). \tag{26}$$

The quantities that specify the BRDF of a given material are the coefficients, A_l^m, of this expansion determined by linear least square fit to laboratory measurements made with the material. The spherical harmonic functions are complex-valued and are defined as

$$Y_l^m=\sqrt{\frac{2l+1}{4\pi}\frac{(l-m)!}{(l+m)!}}P_l^m(\cos(\theta))e^{im\phi}, \tag{27}$$

where P_l^m are associated Legendre polynomials. Rather than the usual complex spherical harmonics, it is actually more convenient to work with real spherical harmonic functions defined as

$$y_l^m(\theta,\phi)=\begin{cases}\sqrt{2}\Re[Y_l^{|m|}(\theta,\phi)] & \text{if } m>0\\ Y_l^o(\theta,\phi) & \text{if } m=0\\ \sqrt{2}\Im[Y_l^{|m|}(\theta,\phi)] & \text{if } m<0,\end{cases} \tag{28}$$

where $\Re(\,)$ denotes the real part and $\Im(\,)$ the imaginary part.[36]

Both the difference angle and the halfway angle can be expressed in these harmonics. Then the transformed BRDF can be expressed as a function

$$\tilde{f}_r(\theta_h,\phi_h,\theta_d,\phi_d)=\sum_{l_h}\sum_{m_h}\sum_{l_d}\sum_{m_d}A_{l_h,l_d}^{m_h,m_d}y_{l_h}^{m_h}(\theta_h,\phi_h)y_{l_d}^{m_d}(\theta_d,\phi_d). \tag{29}$$

The number of m values needed to properly characterize a material is rather small: $m\leqslant 6$ suffices in most cases. By the reciprocity principle the BRDF is the same for interchange of incident and reflected angles, so

$$\tilde{f}_r(\theta_h,\phi_h,\theta_d,\phi_d)=\tilde{f}_r(\theta_h,\phi_h,\theta_d,\phi_d+\pi). \tag{30}$$

The condition implies that all harmonic coefficients with odd values of m_d will be zero. If there is symmetry about the plane of incidence, only the harmonics with non-negative values of m_h will contribute. If the material is isotropic, only harmonics with $m_h=0$ will be nonzero. These symmetry conditions reduce the number of harmonic coefficients that need to be included in the harmonic fits.

Other sets of orthogonal functions such as Zernike polynomials have also been used to characterize BRDF and could have been used to similar effect.[37] Other common methods of empirical BRDF representation such as spherical wavelets[38,39] or nonlinear dimensionality reduction[40,41] were rejected due to their inability to extrapolate over regions lacking experimental data due to the local support of the representation functions.

D. Logarithm fitting and separability

For most materials, the halfway angle and difference angle dependencies are approximately separable, that is,

$$\tilde{f}_r(\theta_h,\phi_h,\theta_d,\phi_d)\Rightarrow f_h(\theta_h,\phi_h)f_d(\theta_d,\phi_h). \tag{31}$$

It is also frequently useful to fit logarithms of the values. This expands the dynamic range that can be fitted effectively. In addition, the separated products can be expressed as a sum,

$$\ln[\tilde{f}_r(\theta_h,\phi_h)f_d(\theta_d,\phi_d)]\Rightarrow\ln[f_h(\theta_h,\phi_h)]+\ln[f_d(\theta_d,\phi_d)]. \tag{32}$$

The form of the spherical harmonic fit then becomes

$$\ln[\tilde{f}_r(\theta_h,\phi_h,\theta_d,\phi_d)]=\sum_{l_h}\sum_{m_h}A_{l_h}^{m_h}y_{l_h}^{m_h}(\theta_h,\phi_h)+\sum_{l_d}\sum_{m_d}B_{l_d}^{m_d}y_{l_d}^{m_d}(\theta_d,\phi_d). \tag{33}$$

This formulation can result in a fit with far fewer harmonics. For example, if ten harmonics are needed to model the halfway angle distribution and ten to model the difference

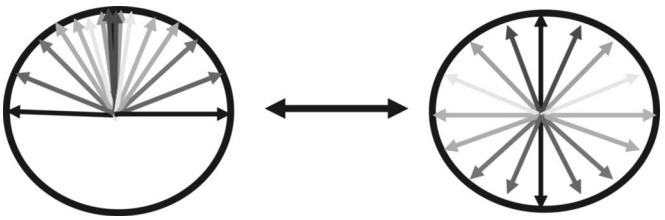

FIG. 5. Effects of angular fan-out.

angle distribution, the total number of harmonics needed is $10+10=20$ rather than the $10\times10=100$ required if the halfway and difference angle dependencies are not separable. Unlike Eq. (29), this separated representation is not guaranteed to fit any conceivable smooth function to arbitrary closeness given a sufficient number of harmonics, but it is quite adequate for most reflectance patterns.

E. Angle fan-out

The region of greatest variation in the BRDF is around the specular peak, where the halfway polar angle, θ_h, is small. Properly resolving the peak can require a large number of spherical harmonics. This requirement can be substantially reduced by transforming the polar angle used for the spherical harmonic fits. The polar angle can be scaled to spread the variation over more of the computational space. Making the transformation

$$\frac{\tilde{\theta}}{180°}=\left(\frac{\theta}{90°}\right)^{\mathrm{se}} \tag{34}$$

fans out the angles near the pole, as depicted in Fig. 5. It also allows for the full sphere modeled by the spherical harmonics to be used to advantage. A scaling exponent of $\mathrm{se}=0.6$ was found to work well. This transformation was used on both the halfway angle and the difference angle, though the main benefit is only with the halfway angle. Unlike the other transformations heretofore described, this technique is not known to have been used in any previous BRDF models.

F. Least squares fitting

In other applications, the spherical harmonic coefficients are computed by taking the integral of their convolution with the complex conjugate of the associated spherical harmonic. That is

$$A_l^m=\int_0^{2\pi}\int_0^{\pi} f(\theta,\phi)\overline{Y_l^m}(\theta,\phi)\sin(\theta)\,d\theta\,d\phi. \tag{35}$$

However, for this process to work properly, the function $f(\theta,\phi)$ needs to be known over the entire sphere.[42] This is not the case in this situation. It is, therefore, necessary to perform a linear least-squares fit to the data. For numerical stability, this needs to be performed using mode-pruned singular valued decomposition methods or constrained least-squares techniques.[43,44]

G. Combined transformations

Many of these techniques have been used in the past to ease the burden of BRDF representation. However, in synergy they have an efficacy beyond their individual virtues. Transforming into halfway angle and difference angle coordinates places the specular lobe along the pole of the spherical harmonic expansion. Angle fan-out then decreases the order of harmonics required. Fitting to the logarithms of values has been done previously, as has treating the BRDF as separable into a product of two functions. However, these techniques are not known to have been used together to reduce the adjustable coefficients required for a spherical harmonic fit. With a lower number of harmonics, the least-square fits are more reliable. Together these techniques allow for efficient representations that are acceptably robust for interpolation, allowing prediction of the reflective behavior of the material at intermediate incident and reflected angles. Light polarization can also be handled by separate fits for both incident and reflected polarizations, but polarization has been ignored for now.

H. Constructing the BRDF from the measured data

A set of spherical harmonic coefficients produced as described above provides a representation of the BRDF at all angles of incidence for a specific state of the surface. Since only one incident angle is used in each test, the results of several tests at different incident angles are required to provide the data needed to produce the required set of harmonic coefficients. Different surface states will have different BRDFs, so the camera frames for each incident angle must be chosen to have the same value of whatever parameter (time, surface temperature, etc.) will be used to distinguish the different surface states.

As computed by the least-squares-fitting routine, the coefficients in the expansion in terms of spherical harmonics represent a best fit to the experimentally observed BRDF. However, the "best fit" is not necessarily the most desirable model for safety calculations. In order to assure safety, a model is desired which always over-predicts the BRDF. If such a conservative fit is desired, the harmonic coefficients can be increased before tabulation to represent a BRDF that is uniformly higher than the measured reflectance for every pair of incident and reflected directions. This is done by adding a base (increasing all values by a fixed amount), increasing values by some multiplier, and broadening the specular peak by assigning a smaller value of the fan-out exponent, se, of the half-way angle to be used when reconstructing the BRDF from the harmonics.

Interpolation is used to predict the BRDF for criteria values other than those tabulated. For example, if harmonic fits are constructed for a material at 100 °C intervals to determine the BRDF at 840 °C, the tabulated BRDF values at 800 °C and 900 °C would be used. Each of the harmonic coefficients would be separately linearly interpolated, in this case taking 60% of the value of the 800 °C tabulation plus 40% of the value of the 900 °C tabulation. Other studies of time-varying BRDF have indicated that time-interpolation of

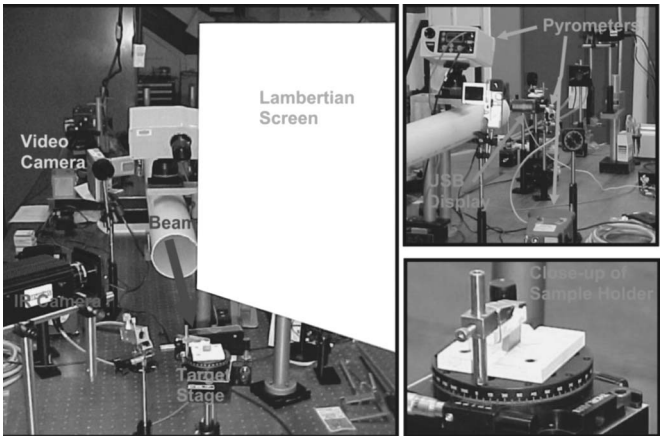

FIG. 6. The laboratory set-up for the testing.

parameters actually yield more accurate results than time-interpolation of the experimental data itself.[45]

Once an appropriate set of harmonics coefficients has been formed by interpolation, the BRDF for any particular angle combination $(\theta_i, \phi_i, \theta_r, \phi_r)$ can be calculated. The procedure is as follows:

(1) Convert the normal $(\theta_i, \phi_i, \theta_r, \phi_r)$ coordinates to the half-way angle and difference angle $(\theta_h, \phi_h, \theta_d, \phi_d)$ coordinate representation, as described in Section IV B;
(2) transform the polar angles using the fan-out factor, as given by Eq. (34);
(3) compute the value for those angles using Eq. (29) [or Eq. (33) if the separable formulation is used];
(4) if the logarithm of the value was stored, take the exponential to get the original value;
(5) divide the result by $\cos(\theta_i)$ and $\cos(\theta_r)$ to form the BRDF [Eq. (17)].

V. DATA

A. Collection procedure

Tests using this dynamic BRDF imaging technique were conducted at AFRL/DE at Kirtland AFB in Albuquerque, NM using a 230 W, 1.06 μm Nd:YAG laser (Fig. 6), the primary samples being stainless steel and copper.[46,47] The samples were $\frac{1}{2}$ inch squares, the stainless steel samples being $\frac{1}{16}$ inches thick and the copper samples $\frac{1}{8}$ inch thick. Most of the samples were irradiated more than once. This was done to distinguish between the reflective properties that are due to the surface temperature and those that are due to the effects of prior irradiation. The BRDF of the samples was a function of the history of the samples, not simply their temperature. For example, a fresh material sample that was heated to 1000 °C for the first time would generally be more reflective than a re-irradiated sample raised to that temperature for a second time due to the production of an oxide layer on the surface of the material after the initial irradiation.

B. Material response

1. General

Both the stainless steel and the copper samples proved to be decidedly anisotropic due to grooves in the surface produced during the machining process. For both copper and stainless steel, there was quite a large sample-to-sample variation in the observed BRDF. At first it was suspected that this might be due to the confusion over the neutral density filters used with the camera, but low power post-test measurements on additional samples showed that there was, indeed, a large sample-to-sample variation in BRDF. For copper samples, normalized peaks and powers for a given incident angle could vary by nearly a power of two. For stainless steel, total reflectance could also vary by almost a factor of two, and peak values could vary by almost an order of magnitude. This variation caused significant difficulty in determining the BRDF variation with incident angle.

A few of the tests were conducted with polarized light. All these tests were conducted at a 40° angle of incidence. While there were some differences between the BRDFs, they were all of the order of the usual sample-to-sample variation. No clear effect of polarization could be determined. Effects might still be present for larger angles of incidence.

Despite the experimental and analytical difficulties, effective analysis proved possible with the copper and stainless steel tests. A qualitative summary of the results is given in Table I.

2. Stainless steel

With stainless steel samples, the reflectance of the materials decreased as the samples were heated. The peak BRDF dropped to a fraction of the initial value, most likely due to the oxidation of the surface, the effect being greater than that normally observed in materials irradiated in a vacuum.[48] After the surface began to melt, the BRDF peak returned to a value close to, or sometimes exceeding, its original value (Fig. 7). Also, the location of the peak moved due to the deformation of the surface. The peak would rise

TABLE I. Qualitative summary of material reflectance behavior.

Effects	Stainless steel	Copper
Early reflectance increase (cleaning)	~10%	~30%
Maximum reflectance	~50%	>90%
Specular peak decrease with heating (oxidation)	Yes	Yes
Specular peak recovers at melting	Yes	No
Specular peak movement during melting	~25%	~5%
Noticeable polarization effects (40° incidence)	No	No

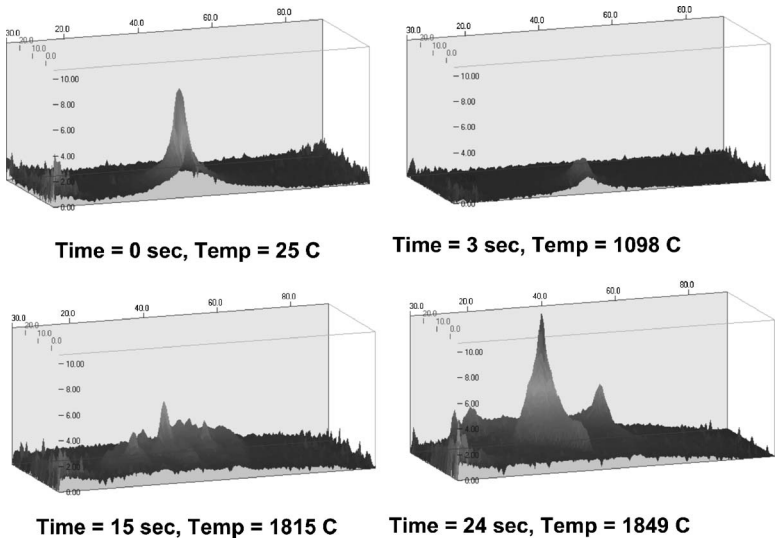

FIG. 7. Evolution of the BRDF pattern for a stainless steel sample.

on the screen as the melted metal slumped down due to gravity. The peak would also wander significantly, varying from moment to moment both in location and magnitude.

3. Copper

When copper samples were irradiated it was generally found that the BRDF initially increased as much as 30% over the starting value. This was likely due to the laser beam cleaning the surface of the metal by burning off contaminants. To a lesser extent, this same effect was sometimes seen with stainless steel samples. With further irradiation, the samples oxidized and the peaks decreased. Unlike stainless steel, melting did not return the copper samples to anywhere near their initial BRDF, as shown in Fig. 8. However, the laser power available in these tests was barely sufficient to melt the copper samples. It is possible that, with higher irradiation, the molten metal might have proved to be more reflective.

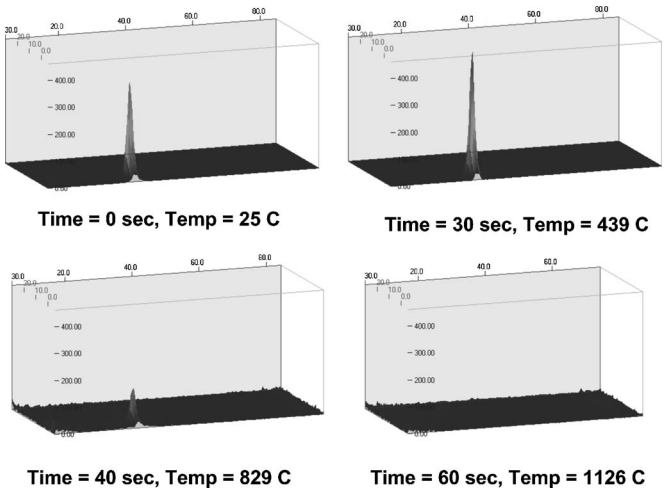

FIG. 8. Evolution of the BRDF pattern for a copper sample.

VI. MODEL APPLICATION WITH EXPERIMENTAL DATA

A. Stainless steel

A spherical harmonic BRDF representation was constructed using data from tests on stainless steel with incident angles of −20°, 0.3°, 5°, 20°, and 40° conducted using test samples with the machining grooves running horizontally. Also included was a test at 20° angle of incidence with the grooves running vertically. The data from the first high power test on each sample was used. Spherical harmonic fits were constructed for times where the temperatures reached 850 °C, the duration of the irradiation varying from 1.09 to 2.66 s to reach this temperature. A single set of harmonics was used to model all incident and reflected angles at each temperature. Values of $l_h \leqslant 8$, $0 \leqslant m_h \leqslant 4$, $l_d \leqslant 2$, and $m_d = 0$ were used for a total of 37 harmonics.

To test the predictive ability of the BRDF fits, data tests at 10° and 30° angles of incidence with horizontal groove orientation and at 40° angle of incidence with vertical groove orientation were set aside and not used in the least squares fitting procedure. Comparisons of the predictions with the actual tests are shown in Figs. 9–11.

Note that the specular peaks are not circular but elongated in one direction. This is due to the tiny grooves created during manufacturing when the metal is rolled. Most BRDF models widely used assume that the materials are isotropic, clearly not the case for these test materials nor most other engineering metals. These fits were able to model this anisotropy. (Without trying to match this effect, 11 harmonics would suffice.) The comparisons were imperfect but well behaved. It was not expected that the fits would match perfectly inasmuch as there was significant sample-to-sample variation in the BRDF. The cumulative test period was too short to allow for multiple tests at most angles of incidence.

To fit to data over a range of temperatures, it is

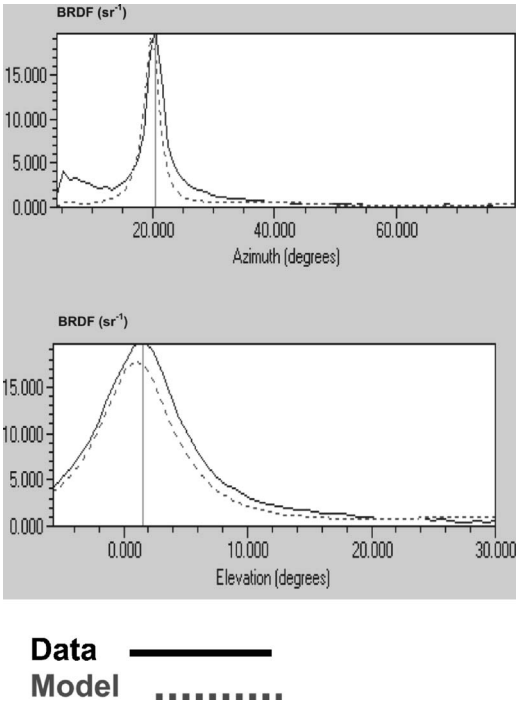

FIG. 9. Comparison of the model and experimental data for 850 °C stainless steel with 10° angle of incidence and horizontal machining grooves.

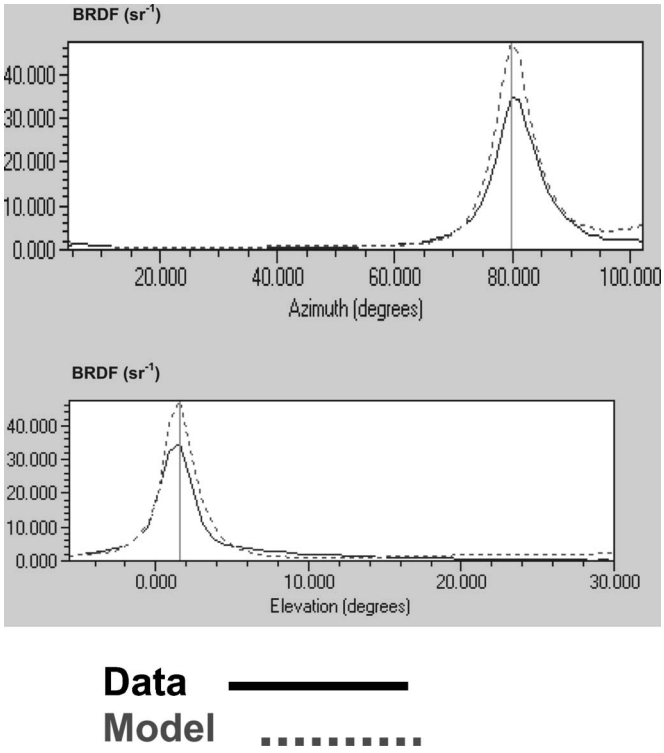

FIG. 11. Comparison of the model and experimental data for 850 °C stainless steel with 40° angle of incidence and vertical machining grooves.

necessary to interpolate harmonic fits for specific tabulated temperatures to intermediate temperatures. This procedure was examined as well. Using the same set of angles and harmonics, a fit was made for the 1050 °C stainless steel surface. An interpolation was constructed to model a 950 °C surface by averaging the values of each of the harmonic coefficients of the 850 °C and 1050 °C cases. Figure 12 depicts the fit to the 10° incident angle at 1050 °C, where both the fit and the comparison data indicate a significantly lower peak than at 850 °C (Fig. 9). Figure 13 then shows a fit constructed by the averaging of two fits, compared against the actual data at 950 °C for a test with a 10° angle of

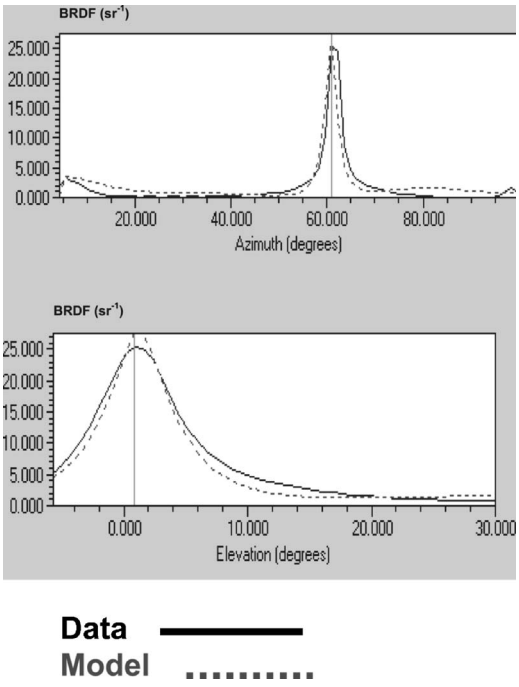

FIG. 10. Comparison of the model and experimental data for 850 °C stainless steel with 30° angle of incidence and horizontal machining grooves.

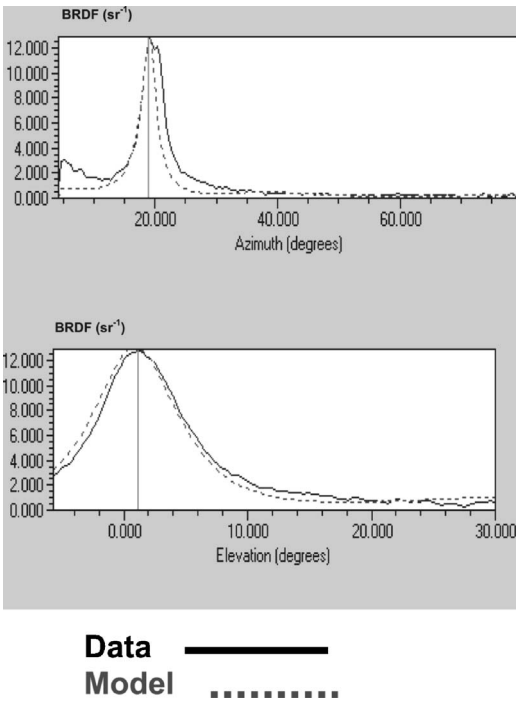

FIG. 12. Comparison of the model and experimental data for 1050 °C stainless steel with 10° angle of incidence and horizontal machining grooves.

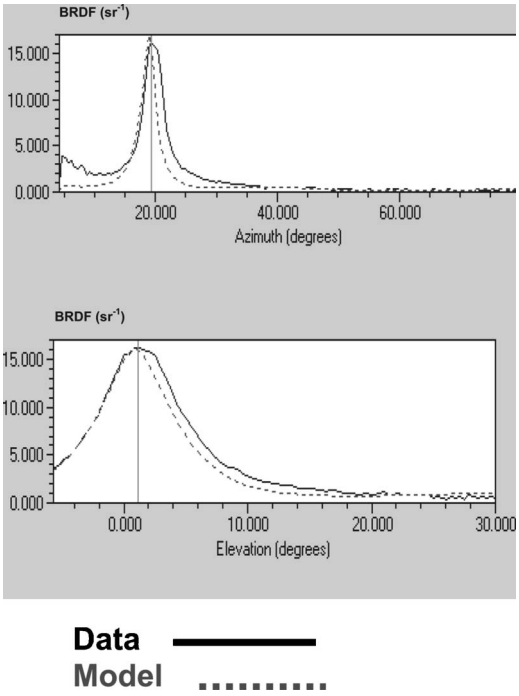

FIG. 13. Comparison of the model and experimental data for 950 °C stainless steel with 10° angle of incidence and horizontal machining grooves. The model prediction is produced by interpolating predictions at 850 °C and 1050 °C.

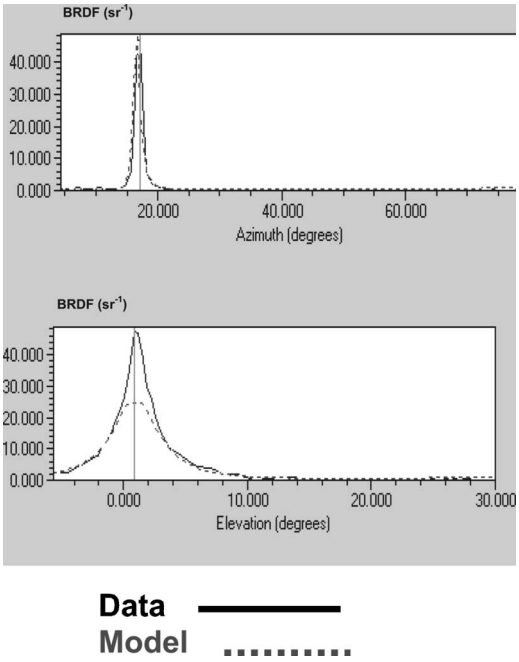

FIG. 14. Comparison of the model and experimental data for 850 °C copper with 10° angle of incidence and horizontal machining grooves.

incidence. Unsurprisingly, where the material response is smooth in its evolution, interpolation to predict intermediate states is an effective procedure.

After the surface melts, the grooving of the surface goes away and the reflection spots are no longer elliptical. As gravity causes the melting metal to flow down the sample, the specular peak on the screen rises, a consequence of the surface normal now pointing upward rather than horizontally. The peaks on the surface also become much less predictable: the points of peak BRDF wax, wane, and wander as the material melts. In situations with other forces on the molten metal (acceleration, airflow, etc.), the primary specular peak displacement might be in other directions rather than the upward direction observed in these experiments.

For the melting case, a similar set of fits to the data were made using the same set of samples, but using the final irradiation of each sample for the material data. Choosing a common temperature to examine results is an ambiguous choice, as the surface temperature of the samples would vary during the period of melting. Instead, a data frame was used for each sample representing the BRDF after 20 s of irradiation, a point at which all the samples were well into the melting regime. The resulting fits are quite poor, badly predicting the BRDF. The reason appears to be the sample variability. Examination of the raw data indicates that there was a large sample-to-sample variation in the BRDF at melting and also a large moment-to-moment variation. This indicates that single sample measurements are unlikely to be sufficient for developing good dynamic BRDF fits: large data sets with sufficient tests to characterize the range of possible response may be required.

B. Copper

A test BRDF fit to the copper data was made similarly to that for the stainless steel data. This did not show any tendency for the BRDF to recover from its low levels prior to melting, so generally the copper was only raised to about 900 °C before ending a test. Also, the pyrometer used for temperature measurement below 800 °C proved unreliable for copper. The result was that there was copper data with reliable temperatures for only a rather small temperature range. This made attempting an interpolation in temperature not very meaningful. However, a BRDF fit was made for data at 850 °C. As with the stainless steel, a fit using incident angles of −20°, 0.3°, 5°, 20°, and 40° was constructed using test samples with the machining grooves running horizontally. Though the grooves in the sample are much finer and less obvious than those in the stainless steel samples, they also produced quite significant anisotropy in the BRDF. Also included was a test at 20° angle of incidence with the grooves running vertically. A single set of harmonics was used to model all incident and reflected angles at each temperature. Values of $l_h \leqslant 10$, $0 \leqslant m_h \leqslant 4$, $l_d \leqslant 2$, and $m_d = 0$ were used for a total of 47 harmonics at each temperature. The resulting set of harmonics was used to predict the expected BRDF at 10° and 30° with horizontal grooves and at 40° with vertical grooves. These predicted values were compared with samples measured at these angles and orientations, as shown in Figs. 14–16.

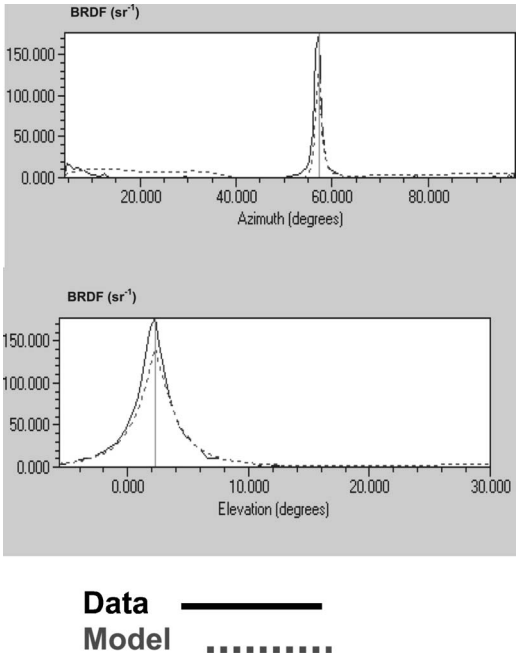

FIG. 15. Comparison of the model and experimental data for 850 °C copper with 30° angle of incidence and horizontal machining grooves.

C. Effects of unsampled regions

One concern has been that only a fraction of the hemisphere is being sampled in determining these harmonic fits. Only about 15% of the total hemispherical solid angle is intercepted by the screen; with symmetry this is equivalent to about 30%. The fitting routine was free to assign any possible values to reflected angles not in the sampled portion of the hemisphere, allowing the creation of spurious reflection lobes in the unsampled regions. This problem was greatly reduced by tacking the BRDF to zero at the horizon (polar angles of 90°) as one of the conditions in the harmonic fitting procedure. These side lobes proved to be a consequence of the anisotropy of the materials: when only $m_h=0$ was used, there were no side lobes, even without forcing the BRDF at the horizon to zero.

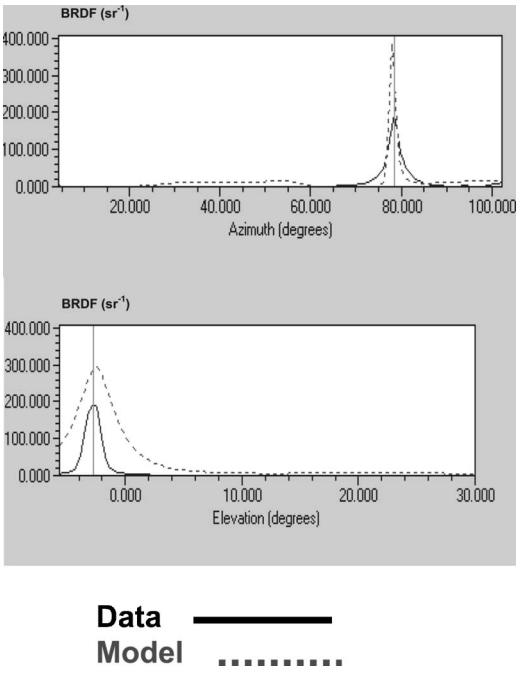

FIG. 16. Comparison of the model and experimental data for 850 °C copper with 40° angle of incidence and vertical machining grooves.

VII. OXIDATION THEORY

The decrease in reflectance that is observed as metals are heated can be modeled using the Wagner theory in which a Fick's Law diffusion of oxygen through the oxide layer is assumed to be the controlling effect.[49–51] In this model, the assumption is made that oxygen must diffuse through the oxide layer for further oxidation and, thus,

$$\frac{dx}{dt} = \frac{\Theta}{x}, \tag{36}$$

where x is the oxide layer thickness and Θ is a temperature-dependent rate function of the form

$$\Theta = \Theta_0 \exp\left(-\frac{T_0}{T}\right), \tag{37}$$

where Θ_0 is a constant. Solving this expression one gets the parabolic law for oxide layer growth

$$x_{j+1} = \sqrt{x_j^2 + \int_{l_j}^{l_{j+1}} \Theta_0 \exp\left(-\frac{T_0}{T}\right) dt}. \tag{38}$$

Due to interference phenomena, the change in reflectance as a function of oxide layer thickness is actually moderately complicated and depends on the electrical-optical properties of the oxide layer. Since these are not known, the assumption is made that the absorptivity of the oxide layer is a simple attenuation, such that

$$R = R_0 \exp\left(-\frac{2x}{a}\right), \tag{39}$$

where R is the reflectance, R_0 is the reflectance in the absence of an oxide layer, and a is an e-folding absorption length for the oxide.

Since neither Θ_0 nor a are known, it is reasonable to parameterize the equation in terms of an extinction parameter:

$$\mu \equiv \frac{2x}{a}, \tag{40}$$

such that

$$R = R_0 \exp(-\mu) \tag{41}$$

and

$$\mu_{j+1} = \sqrt{\mu_j^2 + \int_{l_j}^{l_{j+1}} d_0 \exp\left(-\frac{T_0}{T}\right) dt}, \tag{42}$$

where

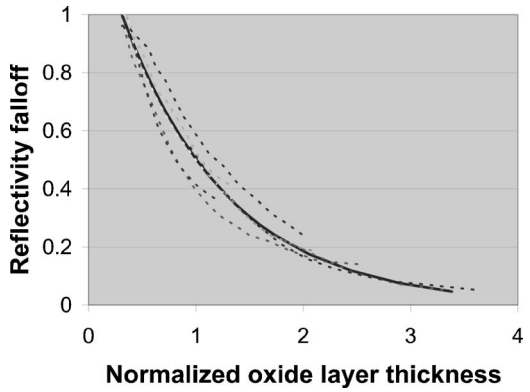

FIG. 17. Fit of stainless steel data to the oxidation model with T_d = 9060 K, μ_0 = 0.311, and d_0 = 935.

$$d_0 = \frac{4\Theta_0}{a^2}. \tag{43}$$

One is then left with three parameters to fit the decrease in the reflectance: the activation temperature T_0, the rate coefficient d_0, and the initial normalized oxide layer thickness μ_0. A fit of the stainless steel data to the oxidation model is shown in Fig. 17.

With copper, it is more difficult to get a good fit using this model. There appears to be other processes underway as well. For the initial phases of heating, the copper becomes more reflective, probably due to the surface being cleaned and polished by the laser beam. However, there also appears to be some process that can remove oxide as well. Previously irradiated samples become more reflective after a few seconds when being irradiated for a second time. If the oxide layer were simply being augmented by the additional heating, one would expect it to decrease, but the opposite is observed.

VIII. CONCLUSIONS

A. Experimental procedure

These tests demonstrated that the BRDF of laser-heated samples with rapidly changing surface properties can be effectively measured by IR imagery of the laser light scattered off the sample surface onto an imaging screen. This technique allows the BRDF pattern for a significant portion of the solid angle about the specular peak to be measured. Infrared pyrometry of the front surface provides a measure of the surface temperature during the laser irradiation. Calibrations using a point source of light allow for compensation for nonideal screen, lens, and IR camera response.

B. Material response

Both copper and stainless steel showed a decrease in reflectance with laser irradiation, apparently due to oxidation of the surface. The surfaces of the samples after being irradiated to a temperature that was high ($>$800 °C) were blackened, rather than shiny like the initial samples. The reflectance decrease was not due to a broadening of the specular peaks but a general decrease at all reflection angles. The reflectance in some cases became so low that it could not be measured accurately using the same camera filters as at the beginning of the test, apparently falling to values of less than 10% of the initial value. This decreased reflectance was clearly not due primarily to the sample temperature: when the samples were allowed to cool and then irradiated again, they displayed the same lower reflectance even in the initial phases of the re-irradiation.

At lower temperatures, samples frequently showed an initial increase in reflectance. This is probably due to sample cleaning. The effect was most significant for copper, with up to 30% increases in reflectance, but smaller 10% effects were also seen with stainless steel.

Upon reaching the melting point, the reflectance of the stainless steel sample changed drastically. The reflectance of the sample recovered and the specular peaks would reach or exceed their initial values. The specular peaks were, however, variable both in size and position.

In contrast, the specular peaks of the copper samples did not reappear upon reaching the melting point. At times, there was a slight increase in the BRDF, but the specular peaks never again reached a value close to those of the early phases of the irradiation. The failure to see the return of the high specular peaks may be due to the fact that there was barely enough power in the laser to reach the melting point with this material; higher laser power might well produce different results.

The differences in the high-energy dynamic BRDF values from the static values were significant and varied from material to material. Testing will be required for each material to be irradiated by high-energy lasers to determine its BRDF under these conditions: no general correction factor can be used to convert static BRDFs to dynamic BRDFs.

C. Representation model

A variety of techniques were used in concert to construct a compact BRDF representation based on limited data. In particular, only a portion of the reflection hemisphere was available for sampling, and data from only limited number of incident angles was available to construct a representation. This implied the need for a data representation in which the reflectance was not a sensitive function of incident angle and which is capable of extrapolation to predict the BRDF in unmeasured regions of solid angle.

This challenge was met by constructing a representation in terms of spherical harmonics in a transformed function space. A variety of additional techniques (angle fan-out, logarithmic representation, etc.) were used in a coordinated fashion to produce representations that are sufficiently detailed and robust to be usable for characterizing the BRDF at all incident and reflected angles.

Each analytic representation required the use of data from multiple experimental tests matched on the basis of common surface temperature. With representations at two surface temperatures, it was shown that the expected BRDF

at intermediate temperature values could also be constructed by interpolation. However, this would only work adequately in situations where the laser power is fairly constant. With a more powerful laser, less time is required to reach a given temperature and the surface is less oxidized and, hence, more reflective. For the stainless steel samples, the modeled thickness of metal oxide on the surface (prior to melting) provides a better measure of the surface reflectance changes than surface temperature.

Dynamic BRDF representation can be constructed as a set of spherical harmonic fits for various surface states (described in terms of temperature, oxidation levels, or other parameters) which are interpolated to predict the BRDF for any desired state. However, current laser safety codes are not easily modified to use time-varying BRDFs. For near-term predictions, "envelope" representations of the BRDF can be constructed which bound the maximum BRDF expected for the material at any thermal state. While these representations significantly over-predict the BRDF, they should be adequate for most safety calculations with high-energy lasers. For high-energy lasers where more accurate BRDF calculations are needed to minimize "keep-out" zones, true dynamic representations are likely to be required.

D. Significance

The dynamic changes in the BRDF that are observed for materials exposed to high-energy laser radiation imply that static BRDF analysis is insufficient to predict the reflections from objects composed of these or similar materials at high irradiance. Even more importantly, the reflectance can be greater and the angle of the specular peak can wander, impacting observers that would be judged to be safely outside the specular peak in a static BRDF analysis. As such, hazard analysis based on static BRDF measurements is insufficient for assuring laser safety when dealing with reflections from high-energy lasers.

[1]F. E. Nicodemus, J. C. Richmond, J. J. Hsia, L. W. Ginsberg, and T. Limperis, "Geometrical considerations and nomenclature for reflectance," National Bureau of Standards (U.S.) Monograph, 1977, p. 160.

[2]X. Feng, J. R. Schott, and T. Gallagher, "Comparison of methods for generation of absolute reflectance-factor values for bidirectional reflectance-distribution function studies," Appl. Opt. **32**, 1234–1242 (1993).

[3]C. Martínex-Antón and E. Bernabeu, "Automatic three-dimensional spectrogoniometer for determination of optical properties and surface parameters," Appl. Opt. **33**, 6059–6061 (1994).

[4]E. Proctor and P. Y. Barnes, "NIST high accuracy reference reflectometer-spectrophotometer," J. Res. Natl. Inst. Stand. Technol. **101**, 619–627 (1996).

[5]D. White, P. Sounders, S. J. Bonsey, J. van de Ven, and H. Edgar, "Reflectometer for measuring the bidirectional reflectance of rough surfaces," Appl. Opt. **37**, 3450–3454 (1998).

[6]V. Havran, A. Neumann, G. Zotti, W. Purgathofer, and H. Seidel, "On cross-validation and resampling of BRDF data measurements," Proceedings of the 21st Spring Conference on Computer Graphics (ACM Press, New York, 2005), pp. 161–168.

[7]H. Li, S. C. Foo, K. E. Torrance, and S. H. Westin, "Automated three-axis gonioreflectometer for computer graphics applications," Opt. Eng. **45**, 043605 (2006).

[8]*Standard Practice for Angle Resolved Optical Scatter Measurements on Specular or Diffuse Surfaces* (American Society for Testing and Materials, West Conshohocken, PA, 1996), Standard E 1392-96.

[9]R. Lu, J. J. Koenderink, and A. M. L. Kappers, "Optical properties (bidirectional reflection distribution functions) of velvet," Appl. Opt. **37**, 5974–5084 (1998).

[10]S. R. Marchner, S. H. Westin, E. P. E. Lafortune, K. E. Torrance, and D. P. Greenberg, "Image-based BRDF measurement including human skin," Proceedings of 10th Eurographics Workshop on Rendering, 1999, pp. 134–152.

[11]W. Matusik, H. Pfister, M. Brand, and L. McMillan, "Efficient isotropic BRDF measurement," Proceedings of the 14th Eurographics Workshop on Rendering, 2003, pp. 241–247.

[12]K. Tonsho, Y. Akao, N. Tsumura, and Y. Miyake, "Development of gonio-photometric imaging system for recording reflectance spectra of 3D objects," Proc. SPIE **4663**, 370–378 (2001).

[13]J. R. Shell II, C. Salvagio, and J. R. Schott, "A novel BRDF measurement technique with resolution-dependent spectral variance," Proceedings of IGARSS, IEEE International, 2004, Vol. 7, pp. 4754–4759.

[14]T. Y. Wu, W. C. Ma, Y. Y. Chuang, B. Y. Chen, and M. Ouhyoung, "Image-based BRDF acquisition for non-spherical objects," Proceedings of 2005 Workshop Computer Vision & Graphics, 2005.

[15]J. Gu, C. I. Tu, R. Ramamoorthi, P. Belhumeur, W. Matusik, and S. Nayer, "Time-varying surface appearance: Acquisition, modeling and rendering," ACM Trans. Graphics **25**, 762–771 (2006).

[16]G. J. Ward, "Measuring and modeling of anisotropic reflection," Comput. Graph. **26**, 265–272 (1992).

[17]S. Wadman and S. Bäumer, "Appearance characterisation by a scatterometer employing a hemispherical screen," Proc. SPIE **5189**, 163–173 (2003).

[18]R. J. Castonguay, "A new generation high speed, high resolution, hemispherical scatterometer," Proc. SPIE **1995**, 152–165 (1993).

[19]P. Mattison, M. Dombrowski, J. Lorenz, K. Davis, H. Mann, and B. Foos, "The hand-held directional reflectometer: An angular imaging device to measure BRDF and HDR in real-time," Proc. SPIE **3246**, 240–251 (1998).

[20]K. J. Dana, "BRDF/BTF Measurement Device," Proceedings of the Eighth IEEE International Conference on Computer Vision, 2001, pp. 460–466.

[21]K. J. Voss, A. Chapin, M. Monti, and H. Zhang, "Instrument to measure the bidirectional reflectance distribution function of surfaces," Appl. Opt. **39**, 6197–6206 (2000).

[22]C. L. Wyatt, *Radiometric System Design* (Macmillan, New York, 1987), Sec. 3.24.

[23]K. E. Torrance and E. M. Sparrow, "Theory of off-specular reflection from roughened surfaces," J. Opt. Soc. Am. **57**, 1105–1114 (1967).

[24]R. L. Cook and K. E. Torrance, "A reflectance model for computer graphics," ACM Trans. Graphics **1**, 7–24 (1982).

[25]M. Oren and S. K. Nayar, "Generalization of Lambert's reflectance model," Proceedings of the 21st annual conference on computer graphics and interactive techniques (ACM Press, New York, 1994), pp. 239–246.

[26]J. J. Koenderink, A. J. van Doorn, K. J. Dana, and S. Nayar, "Bidirectional reflection distribution function of thoroughly pitted surfaces," Int. J. Comput. Vis. **31**, 129–144 (1999).

[27]J. R. Maxwell, J. Beard, S. Weiner, D. Ladd, and S. Ladd, "Bidirectional reflectance model validation and utilization," Technical Report AFAL-TR-73-303, Environmental Research Institute of Michigan (ERIM) (1973).

[28]H. B. Westlund and G. W. Meyer, "A BRDF database employing the Beard-Maxwell reflection model," Graphics Interface **2002**, 201–208 (2002).

[29]S. K. Nayar, K. Ikeuchi, and T. Kanade, "Surface reflection: Physical and geometric perspectives," IEEE Trans. Pattern Anal. Mach. Intell. **13**, 611–634 (1991).

[30]X. D. He, K. E. Torrance, F. X. Sillion, and D. P. Greenberg, "A comprehensive model for light reflection," Comput. Graph. **25**, 175–186 (1991).

[31]B. T. Phong, "Illumination for computer generated graphics," Commun. ACM **18**, 311–317 (1975).

[32]E. P. F. Lafortune, S. C. Foo, K. E. Torrance, and D. P. Greenberg, "Non-linear approximation of reflectance functions," Comput. Graph. **31**, 117–126 (1997).

[33]S. M. Rusinkiewicz, "A new change of variables for efficient BRDF representations," *Eurographics Rendering Workshop*, 1998, pp. 11–22.

[34]S. H. Westin, J. R. Arvo, and K. E. Torrance, "Prediction reflectance functions from complex surfaces," Comput. Graph. **23**, 255–264 (1992).

[35]J. Kautz, P. Sloan, and J. Snyder, "Fast arbitrary BRDF shading for low-frequency lighting using spherical harmonics," *Thirteenth Eurographics Workshop on Rendering*, 2002, pp. 291–297.

[36]H. H. Homeier and E. O. Steinborn, "Some properties of the coupling coefficients of real spherical harmonics and their relation to Gaunt coefficients," J. Mol. Struct.: THEOCHEM **368**, 31–37 (1996).
[37]J. J. Koenderink and A. J. van Doorn, "Phenomenological description of bidirectional surface reflection," J. Opt. Soc. Am. A **15**, 2903–2912 (1998).
[38]P. Schröder and W. Sweldens, "Spherical wavelets: Efficiently representing functions on a sphere," Comput. Graph. **26**, 255–264 (1992).
[39]P. Lalonde and A. Fournier, "A wavelet representation of reflectance functions," IEEE Trans. Vis. Comput. Graph. **3**, 329–336 (1997).
[40]O. G. Cula and K. J. Dana, "Compact representation of bidirectional texture functions," *Proceedings of the 2001 IEEE Computer Science Conference on Computer Vision and Pattern Recognition*, 2001, pp. I-1041–I-1047.
[41]W. Matusik, H. Pfister, M. Brand, and L. McMillan, "A data-driven reflectance model," ACM Trans. Graphics **22**, 759–769 (2003).
[42]W. Saunders and B. E. Ballinger, "Interpolation of discretely-sampled density fields," Astron. Soc. Pac. Conf. Ser. **218**, 181–186 (2000).
[43]W. H. Press, S. A. Teulkolsky, W. T. Vetterling, and B. P. Flannery, *Numerical Recipes in C, Second Edition* (Cambridge U.P., Cambridge, 1992), pp. 59–70, 671–681.
[44]P. M. Lam, C. S. Leung, and T. T. Wong, "Noise-resistant fitting for spherical harmonics," IEEE Trans. Vis. Comput. Graph. **12**, 254–265 (2006).
[45]J. Gu, C. I. Tu, R. Ramamoorthi, P. Belhumeur, W. Matusik, and S. Nayer, "Time-varying surface appearance: Acquisition, modeling and rendering," ACM Trans. Graphics **25**, 762–711 (2006).
[46]A. W. Bailey, K. S. Keppler, V. Villavicencio, D. V. Seaman, R. A. Gallaway, R. J. Thomas, P. Kennedy, M. Mayo, and G. Megaloudis, "A preliminary evaluation of dynamic bidirectional reflectance distribution function testing and modeling," United States Air Force Research Laboratory Report AFRL-HE-BR-TR-2004-0153 (2004).
[47]A. W. Bailey, E. A. Early, K. S. Keppler, V. I. Villavicencio, J. J. Zohner, G. Megaloudis, R. J. Thomas, and P. Kennedy, "Dynamic bidirectional reflectance distribution function testing and modeling," United States Air Force Research Laboratory Report AFRL-HE-BR-TR-2005-0160 (2005).
[48]R. Freeman, F. Rigby, and N. Morley, "Temperature-dependent reflectance of plated metals and composite materials under laser irradiation," J. Thermophys. Heat Transfer **14**, 305–312 (2000).
[49]A. M. Prokhorov, V. I. Konov, I. Ursu, and I. N. Mihăilescu, *Laser Heating of Metals* (Adam Hilger, Bristol, 1990), pp. 140–186.
[50]I. Ursu, L. Nanu, and I. N. Mihăilescu, "Diffusion model for the laser oxidation of metallic samples in air," Appl. Phys. Lett. **49**, 109–111 (1986).
[51]L. Baufay, F. A. Houle, and R. J. Wilson, "Optical self-regulation during laser-induced oxidation of copper," J. Appl. Phys. **61**, 4641–4651 (1987).